Passive Localization of Medical Intubation Tips Using Phonon Crystals

Yi Luo[1, a)], Xiangjun Zhang[1, b)]

[1]*Tsinghua University, Beijing, 100084, China*

[a)] y-luo23@mails.tsinghua.edu.cn
[b)] Corresponding author: xjzhang@mail.tsinghua.edu.cn

Abstract. Intubation operations outside the hospital and at the bedside require rapid, intuitive and reproducible tip positioning capabilities. Traditional imaging methods that rely on large-scale equipment are difficult to invoke in emergency scenarios. Ultrasound, on the other hand, has advantages such as portability, real-time performance, and safety. However, under complex tissue/catheter interface conditions, the stable visibility of the tip is still insufficient. Phonon crystals demonstrate extraordinary potential in longitudinal sound wave propagation. By designing their size and structure, acoustic band gaps of specific frequencies can be obtained, and wireless long-distance sensing and positioning can be further achieved, providing a brand-new idea for the positioning of intubation tips. To this end, this paper proposes and validates a passive ultrasonic marker based on phonon crystals, which is integrated into the tip of medical catheters and achieves frequency-selective narrowband reflection through a Bragg band gap, thereby enhancing contrast and providing recognizable spectral features in conventional B-mode. The marker adopts a cylindrical circumferential periodic hole array (CPC), which is composed of a biocompatible flexible substrate (such as PDMS/ silicone) and an air cavity. The typical outer diameter is approximately 8mm and is compatible with adult catheter specifications (about 24Fr). Experiments have proved that by combining small ultrasonic imaging equipment, characteristic signals can be detected under human-like tissues, achieving wireless positioning during the intubation process. This study demonstrates the passive, integrable and frequency-coded positioning concept of "ultrasonic +CPC", and reveals the potential of flexible CPC to be pressure-sensitive and map the force as a bandgap frequency shift, laying the foundation for subsequent force feedback and adhesion monitoring.

INTRODUCTION

Medical professionals usually insert catheters into the target blood vessels and related anatomical areas within the human body. Once the tip of the catheter is accurately positioned in the predetermined target blood vessel area, various treatment and support measures can be implemented, such as the infusion of chemotherapy drugs [1,2], establishment of extracorporeal circulation [3], hemodynamic monitoring [4], and other endovascular treatments [5]. Extracorporeal membrane oxygenation (ECMO) plays a key role in the treatment of acute cardiovascular events and respiratory failure [6,7], and can be used as independent treatment, adjuvant treatment or transitional treatment [8]. In situations where resources such as out-of-hospital emergency care and various bedside operations are limited, how to complete intubation quickly and reliably [9] and accurately confirm the tip position of the catheter (insertion) while minimizing ionizing radiation and reliance on complex equipment is the core link that determines the effectiveness of treatment and the risk of complications. However, if the tip of the catheter is improperly positioned during insertion or misaligned after insertion, it may cause complications, including patient safety risks, increased risk of thrombosis, delayed treatment delivery, abnormal catheter function, and additional medical costs. The appropriate catheter insertion criteria depend on the type of catheter and the therapeutic purpose. Different modes and approaches also have clear anatomical requirements for the tip position. For example, in VV-ECMO, the reinfusion and drainage catheters need to be located in specific cardiac cavity/large vein regions respectively [10], while VA-ECMO needs to take into account both arteriovenous pathways and hemodynamic safety boundaries [11]. Under emergency or complex conditions, it is not uncommon for tips to mistakenly enter non-target vascular branches or migrate after

surgery, which is associated with risks such as hemodynamic disorders, thrombosis/embolism, bleeding, and treatment delays [12]. The incidence of complications reported in the past has a wide range, ranging from 10% to 50%, and is affected by factors such as patient composition, device type, guidance method and central experience [13,14]. Therefore, for ECMO intubation outside the hospital and at the bedside, establishing a tip positioning protocol that does not require ionizing radiation, has a simple process, is repeatable, and imposes a low burden on the operator is of great clinical significance.

Image guidance is currently the most important positioning path. In terms of availability and application maturity, relevant research and clinical practice have focused on five types of imaging methods: real-time magnetic resonance imaging (MRI), computed tomography/angiography (CT/CTA), photoacoustic imaging (PA/PAI), digital subtraction angiography (DSA), and ultrasound imaging (US). Lederman et al. achieved catheter navigation and precise intramural myocardial injection using real-time magnetic resonance imaging (MRI) in 2002 and Nazarian et al. in 2008 [15]. Dong et al. further integrated multi-core FBG deformation reconstruction with MRI-guided robots in 2022 [16]. It can obtain the "position + shape" of the catheter in real time within the same coordinate system and complete the target hit and path tracking through closed-loop control. MRI can provide high soft tissue contrast without ionizing radiation and support active/passive labeling and morphological feedback of devices. However, it has high equipment size and cost, strict compatibility and safety requirements, and obvious frame rate and SAR constraints, making it difficult to be used outside hospitals or at regular bedside [17]. CT/CTA can quickly present anatomical and lesion coordinates in emergencies, making it suitable for "pre-localization" and path decision-making. In 2022, Tse et al. used a cohort of lower gastrointestinal bleeding with positive localization by computed tomography angiography (CT/CTA), but there was a burden of ionizing radiation and contrast agents, and it was difficult to achieve continuous real-time tip tracking [18]. DSA, as the intraoperative gold standard for interventional therapy, can stably develop images and provide real-time guidance under fluoroscopy, but it relies on X-rays and contrast agents, and has high requirements for site and team configuration [19]. Photoacoustic imaging shows potential in providing structure-functional information and deep microcirculation assessment, but due to the limitations of optical channels and equipment configuration, the normalization and out-of-hospital adaptation are still advancing [20]. Based on the existing research, the mode of in vivo passive sensing combined with in vitro monitoring has significant advantages in terms of continuity, safety and convenience. However, in vitro monitoring methods such as photoacoustic imaging and magnetic resonance imaging require huge equipment, and the possibility of miniaturization is small, which has significant limitations in terms of the convenience of monitoring.

Ultrasonic sensing is a sensing technology based on ultrasonic waves, which can penetrate human tissues and measure information about human physiology or tissue structure [21]. Due to the excellent spatial resolution of ultrasound detection in deep tissues, it can continuously monitor the physiology of deep human tissues in a non-invasive manner, including organ signals and dynamics, or key information related to health and disease. In contrast, ultrasound has comprehensive advantages such as non-ionizing radiation, portability, accessibility, controllable cost and repeated use at the bedside. It is generally regarded as a more feasible preferred imaging method for ECMO intubation outside the hospital and at the bedside [22,23,24].

However, in the deep, long-path and postural restricted scenario of ECMO intubation, ultrasound imaging faces multiple challenges: at a large imaging depth, a lower frequency band needs to be used at the expense of resolution; Shadows and artifacts, speckle noise and sidelobe interference caused by bone and gas occlusion can all reduce image clarity [25]; The specular reflection on the metal or polymer surface of the guide (plug-in) tube makes the "direct viewing" of the tip highly dependent on the incident Angle, which is prone to "Angle disconnection" and sharp contrast drop [26]; Operator dependence also affects stability and repeatability [27,28]. Under the conditions of time pressure and limited operating space outside the hospital and beside the bed, it is often difficult to continuously and intuitively confirm the tip position in different directions and depths solely relying on conventional ultrasound.

To enhance the visibility of the tip under ultrasonic conditions, previous work has mainly explored acoustic contrast enhancement along two paths: one is to form a strong echo cloud in the heart cavity/blood vessels by stimulating physiological saline or ultrasonic microbubbles [29] (UCA) to infer the cavity where the tip is located, the patency of the channel, and the risk of accidental entry; Ultrasonic microbubbles are blood pool contrast agents filled with inert gas and coated with proteins or phospholipid shells. They generate nonlinear oscillations under low sound pressure, significantly enhancing the acoustic signal ratio of blood to tissue and facilitating acoustic separation and development. As early as 1984, Widder and Simeone verified the feasibility of ultrasound-guided puncture and shunt catheter operation using the "ventriculo-cyst" model [30]. Microbubbles generated by hand injection of a small amount of normal saline can form a strong echo cloud in the capsule cavity/ventricle, clearly indicating the intracavitary or extracavitary position of the needle/tube end. It can determine whether the multi-lumen compartments are connected. The microbubble extravasation path can also be used to judge the patency of the catheter side holes and whether the

catheter has mistakenly entered the outside of the lumen. In 2017, Da Hora Passos et al. used "stimulated normal saline microbubble enhanced ultrasound" [31] to identify whether the catheter mistakenly entered the ipsilateral internal jugular vein, axillary vein, other veins, etc., and could track the direction of the catheter in combination with ultrasound above and below the neck/clavicle. This approach is simple to operate and has significant enhancement, but the signal duration is limited, repeated injection is required, and it is affected by blood flow, occlusion and individual acoustic window differences.

The second approach is to use echogenic surface/coating (echogenic surfaces/UEC) [32,33] to enhance scattering and angular tolerance by immobilizing/capturing gas, constructing micro-cavities or regular textures; In addition, phase change precursors such as perfluorocarbon nanodroplets [34] can also be confined within surface or cavity structures. Under low to moderate sound pressure, the acoustic droplets can be triggered to vaporize, generating local microbubbles and producing strong nonlinear and harmonic signals [35]. van de Berg et al. [36] found in 2019 that EDM grooving, sawtooth/thread and other textures could significantly broaden the "high-echo Angle range" and achieve higher CNR/SR in standardized evaluations. In application scenarios, when the UEC/ echo-enhanced surface guide needle/instrument enters the capsule cavity, blood vessel or tissue space, a continuous and high-contrast outer wall contour can be formed, which is convenient for determining the "intracavitary/extra cavitary" position. This approach has a clear processing route and has achieved positive results on some equipment. However, its enhanced strength and stability under deep and angular conditions are still limited, and it may introduce engineering constraints in terms of wear resistance, propulsion friction and long-term stability. In scenarios outside the hospital and at the bedside, the ideal solution should minimize additional injection or activation processes to reduce the time and process burden on the operator, while maintaining repeatable and predictable visibility in different directions and depths.

Overall, the feasibility of achieving image enhancement in the surface/structure field has been supported by experiments and theories [37], but animal/clinical-grade verification for catheters still needs further development. There are relatively few publicly available results on mass-produced ultrasonic-enhanced coatings for catheter localization, and most are still in the development or research stage.

Based on the above motives, this paper explores a passive structural labeling scheme different from the imaging and coating paths: integrating a cylindrical phononic crystal (cylindrical phononic crystal, CPC) inside the tip of the conduction (insertion) tube as a passive acoustic labeling. Phonon crystals are a type of acoustic metamaterial implementation that generates Bragg scattering and forms a band gap through geometric periodicity. They exhibit transmission suppression and strong backscattering for incident sound waves within a specific frequency band [38]. By constructing a subwavelength circumaxial periodic air hole array within a flexible and biocompatible elastic matrix, CPC can tune its bandgap center and width through geometric parameters within the commonly used 1-5 MHz window in clinical practice, thereby matching the preset ultrasound probe and imaging depth during ECMO intubation. Cylindrical symmetry and circumferential periodicity enable it to maintain a high echo intensity within a wide azimuth range, alleviating the dependence of tip visualization on the incident Angle. Unlike the approach of injecting contrast agents or constructing wear-prone textures on the surface of the device, CPC achieves narrowband and predictable frequency selectivity enhancement through an embedded structure, taking into account the requirements of passivity, stability and process simplicity. Meanwhile, this approach is complementary to microbubbles/coatings in clinical practice and can be selected based on resource conditions and operational objectives.

The work of this paper centers on the goal of "bedside/out-of-hospital accessible ultrasound guidance", and proposes and validates the idea of CPC passive labeling integrated at the tip of ECMO intubation: at the conceptual level, it clearly takes the Bragg band gap as the core mechanism to achieve structure-band engineering tuning for the 1-5 MHz clinical frequency band; At the verification level, the design is guided by the combination of energy band and transmission analysis, and the improvement of tip image contrast and echo signal-to-noise ratio is evaluated based on the conventional bedside ultrasound preset under the conditions of water trough and tissue equivalent volume model. At the control level, it is compared with unlabeled tips and typical enhancement methods to demonstrate its visible stability and operational feasibility in complex positions and depths. We expect this passive and structural acoustic marker to provide more reliable tip positioning guarantee for ECMO intubation in out-of-hospital emergency care and various bedside operations, and lay the foundation for subsequent standardized and large-scale manufacturing for clinical processes.

MATERIALS AND METHOD

In this study, cylindrical phononic crystals (CPC) were used as passive acoustic markers at the tip of ECMO tubes, and structural design, numerical simulation, sample preparation and ultrasonic verification were carried out with the

goal of "adjustable band gap, Angle/azimuth robustness, and matching with bedside ultrasonic frequency bands". Considering that single-phonon crystals typically form only 1-2 major Bragg band gaps within the target frequency band, making it difficult to cover the entire 1-5 MHz clinical window, we adopt a segmented layout strategy in engineering: Multiple CPC segments are configured at different axial positions of the guide (insert) tube, and the geometric parameters of each segment are tuned to different center frequencies respectively, so that they can be perceived under different probe and depth presets.

Phonon Crystal CPC Structure and Design Strategy

The CPC is cylindrical in shape, which is convenient for insertion at the end of the conduit. As shown in the Figure 1, the interior adopts a two-dimensional square lattice air hole array, which repeats along the circumferential direction to form a ring-shaped hole row and repeats along the axial direction in a finite number of layers. The outermost ring band is partially thickened for structural stability and encapsulation. The analysis at the band level is carried out using two-dimensional square lattice cells for Bloch-Floquet calculations. The approximate basis is the local plane assumption: when the lattice constant a is much smaller than the cylindrical radius R ($a \ll R$), the circumaxial curvature can be ignored within the single-cell scale, and the dispersion relationship of the planar lattice can reasonably predict the position and width of the local Bragg band gap. The cylindrical curvature and the finite-length effect were subsequently verified and corrected in the finite-period transmission simulation and experiments. The design variables include the lattice constant a, pore size d, filling ratio $\varphi=d^2/a^2$ (square lattice), circumferential period N_θ and axial period N_z. According to the first-order Bragg condition, the bandgap center frequency f_0 approximately satisfies $f_0 \propto$ ceff/(2a) with the equivalent phase velocity ceff and the period a. When the material is fixed, a controls the band gap translation, while d/a and ϕ mainly affect the band gap width and depth. To match the bedside imaging, we selected representative frequency points located at 2-3 MHz for tuning and sample preparation. Meanwhile, several typical points within the 1-5 MHz range were covered in the simulation to evaluate the universality.

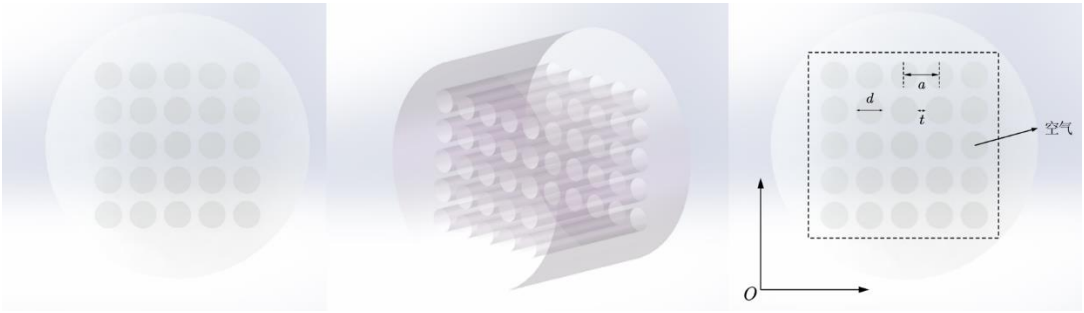

FIGURE 1. Three-dimensional schematic diagram of cylindrical phonon crystals.

When ultrasonic waves are incident on a CPC with a multi-layer air column structure arrangement, the CPC will exhibit the acoustic bandgap effect of phonon crystals, generating strong reflection of ultrasonic waves within a certain narrowband frequency range. The reflected ultrasonic waves can be re-received by the ultrasonic probe and can be distinguished in the frequency domain from other surrounding tissues, providing potential characteristic signals. Its acoustic bandgap effect, like that of phonon crystals, will change accordingly with the alteration of parameters such as the lattice constant and duty cycle of the internal air column structure.

Phonon Crystal Band Gap Theory and Band Calculation

The core theory of phonon crystals is based on the elastic dynamics equation and Bloch's theorem. According to the elastic dynamics theory, under the premise of basic assumptions such as material continuity, linear elasticity, uniformity, isotropy and small deformation, an arbitrarily small volume element is selected. According to the three basic equations of the relationship between particle force, displacement and stress-strain, The Navier-Cauchy equation can be obtained:

$$\rho \frac{\partial^2 u}{\partial t^2} = \rho f_i + \nabla\left(\lambda + 2\mu\right)\left(\nabla \cdot \boldsymbol{u}\right) - \nabla \times \left(\mu \nabla \times \boldsymbol{u}\right) \tag{1}$$

The solid domain of phonon crystals adopts the assumption of linear elastic small deformation. Equation (1) can be written as:

$$\nabla\cdot\left(C:\nabla u\right)+\rho w^2 u=0 \tag{2}$$

The core feature of phonon crystals is that the material parameter C is a position-dependent fourth-order elastic tensor, which describes the elastic properties of the material in different directions and shows a periodic distribution in space, satisfying:

$$C\left(r+R_1\right)=C\left(r\right) \tag{3}$$

Here, R is the lattice translation vector.

Solving the band structure of the intrinsic frequency $\omega_n(k)$ varying with k is the core of the phonon crystal theory analysis. We perform the calculation through the finite element method (FEM). According to the finite element theory [39], equation (1) can be transformed into a generalized eigenvalue equation with discrete form:

$$\left(K-\omega^2 M\right)u=0\,. \tag{4}$$

Characteristic value ω^2 represents the square of the natural frequency; Eigenvector u represents the corresponding vibration mode (displacement distribution) for phonon crystals.

After finite element discretization of periodic phonon crystals, the overall stiffness and mass matrix present a band-block structure, containing only the coupling between the original cell and its nearest neighbor. According to the Bloch-Floquet theorem, the displacement field satisfies

$$u\left(r+R\right)=u\left(r\right)e^{ikR}\,. \tag{5}$$

Based on this, the infinite periodic domain can be reduced to a single cell calculation.

Thus, a two-dimensional square lattice cell model (side length a, aperture d) was established in the solid mechanics module of Comsol Multiphysics, and Bloch periodic conditions were applied to the relative boundaries. For the two-dimensional square phonon crystal cells, the form of the periodic boundary conditions is as follows:

$$u\left(x+a_1,y\right)=u\left(x,y\right)e^{ik_x\cdot a_1},u\left(x,y+a_2\right)=u\left(x,y\right)e^{ik_y\cdot a_2}, \tag{6}$$

In the formula: -- The basal vector of the protocell; -- The wave vector of the inverted grid space.

And scan the wave vector k along the Γ-X-M-Γ path in the first Brillouin zone, solve the generalized eigenproblem $\left[K\left(k\right)-\omega^2 M\left(k\right)\right]u=0$, obtain the dispersion relation and identify the band gap, as shown in the Figure 2, that is, the band diagram [40]. Grid division is carried out using planar strain triangular elements and it is ensured that there are no less than 10 elements for each minimum wavelength in the matrix. The convergence criterion is taken as the band gap edge frequency variation being less than 1%.

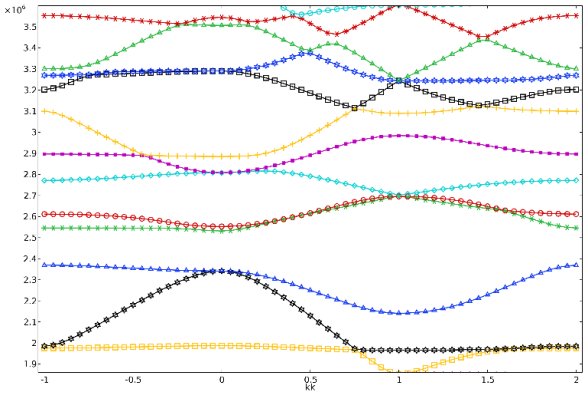

FIGURE 2. Dispersion relationship diagram of the first Brillouin region of a two-dimensional phonon crystal: lattice constant a=0.87, duty cycle =0.78.

Simulation of Finite Period Transmission and Angle/Azimuth Response of phonon Crystals

Through band calculation, we can obtain characteristics such as the band gap position and band gap width of phonon crystals. However, to obtain the specific attenuation of elastic waves by finite structures, we need to further

solve the transmission spectrum (transmission spectrum) of phonon crystals with finite structures. According to the finite element theory, the finite element equation under the condition of acoustic-solid coupling is considered:

$$Kp + M\ddot{p} = Qp \tag{7}$$

K: Stiffness matrix, describing the elastic properties of a crystal.

M: Mass matrix, describing the inertial properties of a crystal.

Qp: External force term, representing the sound pressure at the boundary.

This is the finite element dynamic balance equation applicable to fluid domain calculations. We established the corresponding finite element model in the finite element software Comsol and carried out the transmission characteristics calculation of finite-structured phonon crystals, which can solve the sound pressure distribution inside and at the boundaries of the crystal, as shown in the Figure 3.

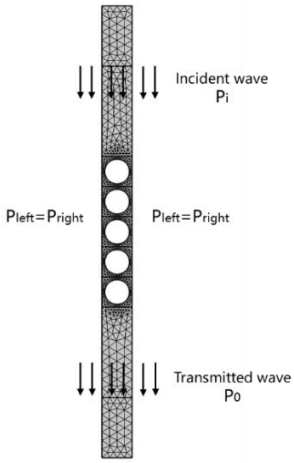

FIGURE 3. Simulation model of Comsol transfer characteristics of phonon crystals.

To evaluate the narrowband transmission suppression and reflection enhancement of a finite-length CPC, the reproducible laboratory process is first completed according to the basic Settings: An equivalent two-dimensional model was built in the Comsol pressure acoustic frequency domain module. The incident surface sound pressure Pi=1 Pa was applied to the upper boundary, the radiation boundary (referring to the sound pressure setting) was used to the lower boundary, and the periodic condition *p*(left)=*p*(right) was applied to the left and right boundaries to simulate an infinite period, as shown in the figure.

In phonon crystal calculations, two parameters, namely the transmission coefficient and the transmission amount, are generally used to characterize the attenuation of sound waves passing through the structure. According to the definition of the transmission coefficient, it is only necessary to calculate the input acoustic energy at the upper boundary and the output acoustic energy at the lower boundary. We integrate the acoustic energy on the two boundaries of the upper line along the edge lines to obtain the input and output acoustic energy of the entire boundary, which has:

$$\omega_i = \int_{\partial\Omega_1} \frac{|p_0|^2}{2\rho c} \mathrm{d}A, \omega_0 = \int_{\partial\Omega_2} \frac{|p|^2}{2\rho c} \mathrm{d}A, \tag{8}$$

p_0: The sound pressure of the incident sound wave. p: The sound pressure of the transmitted sound wave. ρ: The density of the medium. c: The speed of sound wave propagation in a medium. $\partial\Omega_1$: The boundary of the incident sound wave. $\partial\Omega_2$: The boundary of the transmitted sound wave.

Calculate the time-averaged sound intensity flux at the boundary between the incident end and the exit end, obtain the power transmission coefficient T=Pout/Pin, and define the transmission loss TL= -10 log T (dB) based on this. Obtain the transmission spectrum through frequency scanning and identify the high TL intervals within the band gap. Simultaneously conduct time-domain and time-frequency domain visualization to observe the energy attenuation and scattering path of the wave in the hole array. After the calculation is completed, array the y direction to obtain the result as shown in the Figure 4.

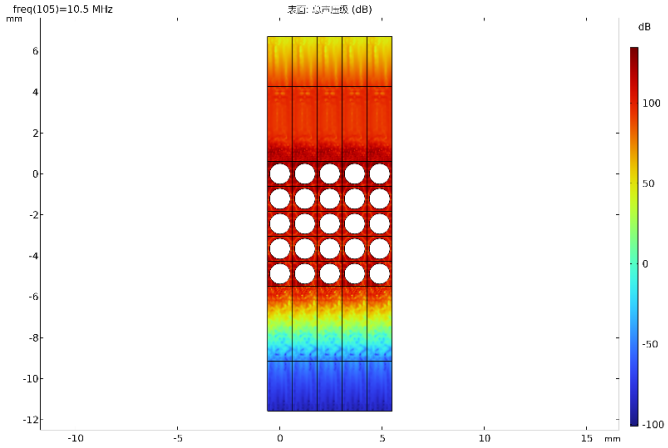

FIGURE 4. Simulation Model of Comsol Transfer Characteristics of phonon crystals (5*5 results).

The results show that the vast majority of the energy is reflected within a specific frequency band, which is consistent with the band gap corresponding to the energy band structure. As shown in the Figure 5, it can be seen that the band gap position of the red dotted line in the band structure diagram is flush with the highest peak in the transmission spectrum on the right, indicating that very few sound waves are transmitted through this frequency band, which confirms the "band gap" of the phonon crystal.

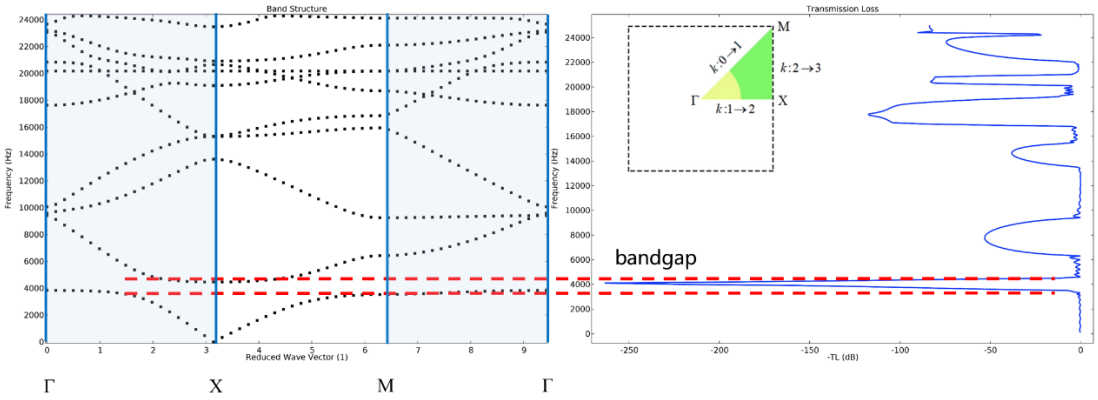

FIGURE 5. Comsol band structure diagram and transmission spectrum of phonon crystals (illustration of other materials used).

Phonon Crystal Design and Preparation

Based on the size parameters studied in the previous text, the phonon crystal structure was drawn using SolidWorks software, and the PDMS and silicone-air system phonon crystals were cast using microneedle-array molds. The aluminum-air system was fabricated by machining. To adapt to the catheter structure, the final shape of the phonon crystal was also designed as a cylinder, as shown in the Figure 6. The flexible samples were prepared by using two types of systems, PDMS - air and medical silica gel - air, through the mold casting process assisted by microneedle array demolding. The prepolymer was mixed in the manufacturer's proportion and degamed (≥ -90 kPa, 5-10 min), then cured in the mold (at room temperature for 24 hours or accelerated at 60-80 °C for 1-2 hours). After demolding, the end face was trimmed and the orifice was encapsulated. All samples are machined into cylindrical sections that can be inserted into the end of the conduit, ensuring axial concentricity and alignment with the end face.

(a) (b)

FIGURE 6. (a) Aluminum - air phonon crystal -A (b) Silica gel - air phonon crystal (left) -C PDMS- Air phonon Crystal (right) -D.

The common specifications of adult ECMO intubation are approximately 13-28 Fr (1 Fr=0.33 mm), with an outer diameter of about 4.3-9.3 mm. The outer diameter of the sample in this article is φ 8mm, approximately equal to 24Fr, which is convenient for matching with the common ends of adult intubations. Other specifications can achieve band-invariant scaling mapping by adjusting the outer diameter and keeping the dimensionless geometry (d/a, φ, N_θ, N_z) unchanged. The CPC section is fixed to the end of the conduit by insertion or bonding, with the end face aligned with the conduit axis. The cavity sealing is regarded as stable during the experimental period in this paper. Long-term packaging and in vivo environmental stability verification are not within the scope of this method.

EXPERIMENT AND RESULT

This section conducts verification around two links: one is the B-MODE imaging link consistent with the clinical process, which is used to evaluate visibility and image contrast; The second is the pulse-echo link, which is used to verify the frequency selectivity and object specificity of the structural origin. All results are mainly expressed in terms of trends and magnitudes to avoid excessive extrapolation of a single value.

Ultrasonic Experimental Platform and Process

The verification involves two links: clinical style B-mode imaging and pulse-echo measurement. The experimental medium was deionized water at 25 °C and tissue equivalent volume model (sound velocity approximately 1540 m/s, attenuation 0.5-0.7 dB/cm/MHz). Before the experiment, the effective sound velocity was calibrated with pulse-echo, and a standard scatterer was placed in the bulk model for system calibration.

B-mode imaging employs a portable/bedside ultrasound host with a 1-5 MHz phased or convex array probe. The center frequency is preset at 2-2.5 MHz based on the target depth and switched to 4-5 MHz when necessary. Fixed gain, TGC, dynamic range and filtering, with compound/enhancement turned off for comparability. The sample is placed in a water tank or body mold, with a distance of 3 to 8 cm between the probe and the sample. The incident Angle θ and the circumferential orientation φ are controlled by the tabletop. θ varies from -60 ° to 60°, and φ varies from 0 to 180°. The data was collected respectively under presets such as 1.5, 2.0, 2.5, 3.0, 3.5, and 4.5 MHz. For each condition, 50 to 100 frames were continuously recorded and averaged within the frames.

The pulse-echo link uses immersion unit transducers (center frequencies 2/2.5/4/5.0 MHz, bandwidth ≥50%), in combination with pulse/receiver (1-3 cycles tone burst, excitation 50-200 V) and high-speed acquisition (≥40 MS/s). Perform echo collection on normal and angular incidence, sweep frequencies within the range of 1-5 MHz, and increase SNR by an average of ≥32 times under each condition. Record the peak value/energy of the gated echo and extract the frequency and angular response curves.

Indicators and Data Processing

The image contrast CNR is calculated on the B-mode image by covering the CPC strong echo area and the adjacent background area with a fixed area ROI respectively. CNR= μs - μb /σb, where μs and μb are the average gray levels of the signal and the background respectively, and σb is the standard deviation of the background. Due to equipment limitations, the RF value of the image cannot be obtained. During the calculation process, a self-written Python script is used to calculate the image. Take the average of each condition over 50 to 100 frames. The echo signal-to-noise ratio (SNR) is calculated by the envelope root mean square (Arms) and noise window root mean square (Nrm) within the time-domain gating window, with SNR=20 log10(Arms/Nrm) (dB). The angular tolerance is defined as the range of incident angles corresponding to when the CNR is not lower than the normal incident CNR threshold (such as 70%) near the bandgap center, and is used to compare the angular robustness of different structures or materials. Frequency-specific analysis aligns the CNR/SNR curve with frequency with the simulated transmission spectrum TL(ω) to test the consistency both inside and outside the band gap.

Experiment 1 Imaging Link (Ultrasonic Development)

To achieve short-term sealing of the air cavity and ensure stability in the water/bulk mold, flexible samples (silicone-air, PDMS-air) are covered with approximately 0.5 mm films at both ends after demolding. The aluminum-air sample is sealed with aluminum end caps installed at both ends. The sample was placed in a water tank or tissue-equivalent phantom. B-mode images were collected using a water-immersed ultrasound probe under a uniform preset to compare the visibility of the "phonon structure" and the "reference", and to evaluate the feature retention after catheter insertion. To evaluate the robustness of Angle and azimuth, a finite length cylindrical CPC section was subjected to an incident Angle change at θ∈[-60°, 60°] and the circumferential azimuth ϕ∈[0°,360°) was rotated with a step size of 10-15 °. The contrast variation with θ and φ was observed to determine the Angle tolerance.

FIGURE 7. Imaging link flowchart.

The samples and controls include: A (aluminum-based CPC, φ 8mm), B (aluminum alloy end cover ×2, no periodic structure reference), C (silicone-based CPC, φ 8mm), D (PDMs-based CPC, φ 8mm), as shown in the Figure 8; Take another section of medical PVC catheter to accommodate A for comparison. In addition, to distinguish the influence of materials and geometry, hollow aluminum tubes and aluminum tubes with periodic pore arrays were prepared as morphological controls simultaneously, as shown in the Figure 9.

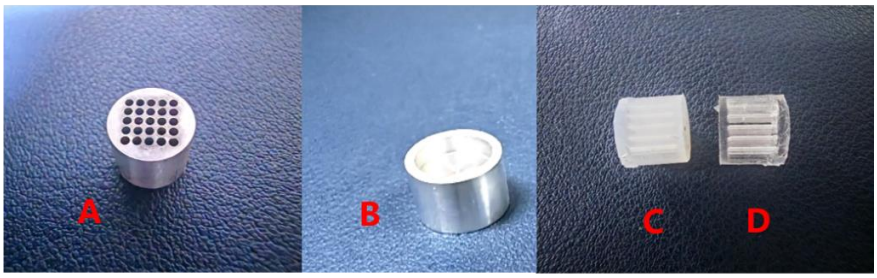

FIGURE 8. Samples A, B, C, D.

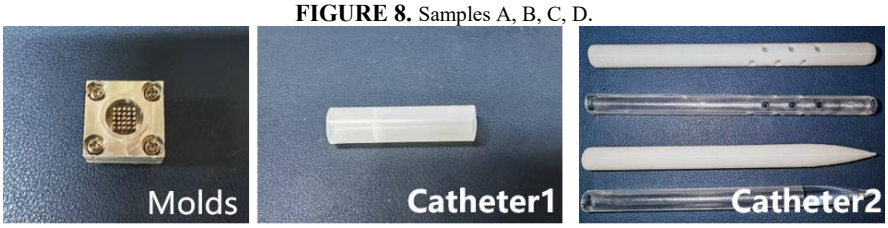

FIGURE 9. The mold and the control catheter.

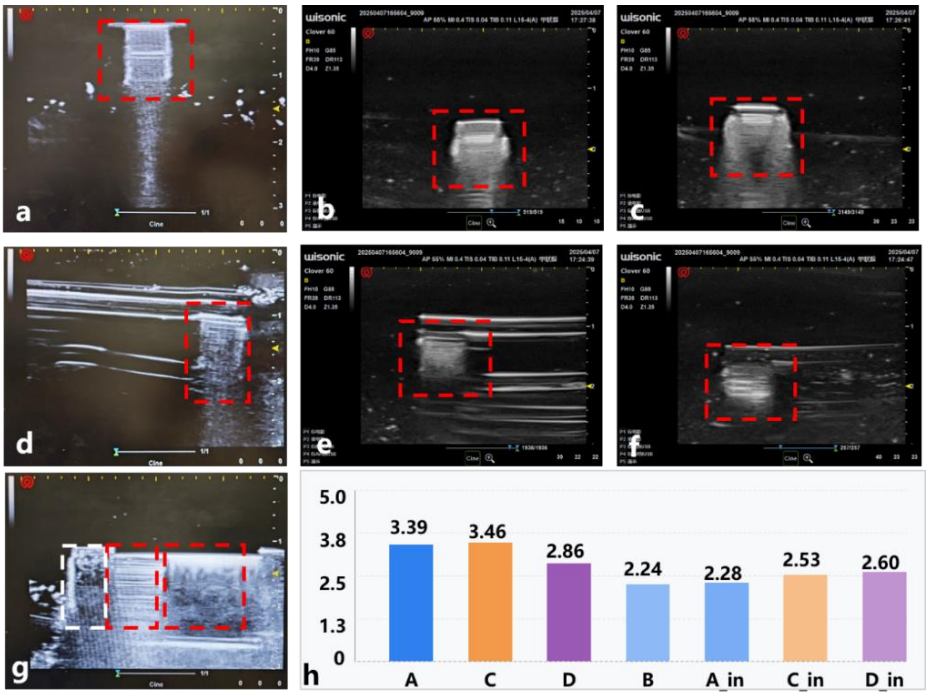

FIGURE 10. Images of different structures under ultrasound imaging. (a) Imaging of a under ultrasound in water; (b) imaging of C under ultrasound, in water; (c) imaging of D under ultrasound in water; (d) imaging of A under ultrasound, in the catheter; (e) imaging of C under ultrasound, in the catheter; (f) imaging of D under ultrasound, in the catheter; (g) Comparison of imaging of A and B under ultrasound. In water, the white box represents B, the middle red box represents A, and the right red box represents a hollow aluminum tube. (h) comparison of CNR values calculated under each imaging.

As shown in the Figure 10, under underwater conditions, A/C/D all exhibit stable and reproducible high-brightness echoes. The periodic structure forms a narrowband and clearly bounded high-contrast feature on the image, while B without periodic reference has weaker echoes and unstable morphology under the same presets. Except for a few Angle/azimuth combinations (commonly seen near grazing incidence or individual φ alignment positions), the normalized CNR of CPC varies little with θ and φ, and remains above the threshold line overall. No obvious periodic fluctuations in φ were observed. The corresponding Angle tolerance covers most of the test Angle intervals, demonstrating strong robustness in incident Angle and azimuth. In contrast, the contrast of B without periodic reference is more prone to fluctuation under the condition of deflection Angle. After A was placed in the PVC catheter, the CNR of each object decreased compared to the exposed state by approximately 0.6 to 1.2 (the order of magnitude estimated by CNR using combined variance), but the characteristics of CPC were still distinguishable, and under the same ROI strategy, its overall CNR was higher than that of B. The review was conducted according to the main analysis definition (CNR = μs - μb / σb) described in the method section, and the conclusion was consistent: CPC maintains a high contrast under a unified imaging preset, while the contrast without periodic reference is more susceptible to attitude and coupling changes. Overall, the imaging link verified that under water and phantom conditions, CPC can obtain visually visible bright spots or bright bands under common presets, and still maintain recognicability under catheter constraints.

Experiment 2: Echo Link (Ultrasonic Signal Acquisition)

This experiment is used to distinguish "object specificity" from "frequency specificity", and verify from the perspective of time/frequency domain whether CPC echo enhancement originates from periodic structure and bandgap effect.

FIGURE 11. Echo link flowchart.

The object-specific test compares the echo responses of CPC-A with multiple controls under the same frequency and equal acoustic pressure conditions to verify whether the enhancement is caused by "periodicity" rather than merely by the material or volume. The controls include: solid controls, random hole controls, hollow catheters, pointed cone catheters and random small hole catheters, etc. The experimental medium is deionized water and tissue-equivalent body mold. Keep the geometry of the sample and the sound field unchanged, and ensure that the sound pressure at the sample is uniform through path compensation and calibration. The frequency is fixed at the representative point (such as 2.5 MHz), and the transmitted/reflected/echo signals are measured and gated and spectral analysis is carried out.

This part is mainly used to verify frequency specificity, Object specificity, and object specificity. To compare the acoustic responses of "phonon crystal A (CPC-A)" with the control substance under the same ultrasonic frequency and equivalent acoustic pressure conditions, and to verify whether the response stems from the periodicity of the structure. The transmission/reflection/echo signals of CPC-A, solid control and random well control were measured respectively in water and tissue equivalent media; Frequency specificity refers to applying different frequencies of incidence (such as 2.0/2.5/4.0/5.0 MHz) to CPC A one by one under the same medium and geometric conditions. Each frequency point is calibrated with equal amplitude at the sample, and the amplitude and spectral characteristics of transmission/reflection/echo are measured. Based on the fundamental mechanism of reflection caused by discontinuous acoustic impedance, the echo arrival time is used to estimate the equivalent depth ($d \approx c \cdot t/2$), as shown in the Fig.12. Spectral analysis is used to capture the energy concentration or frequency shift characteristics related to the band gap. The time-domain signal is first bandpass filtered, and then the root mean square amplitudes Arms and Nrm are calculated respectively in the gating window and the terminal noise window of the target echo. This definition is consistent with the method part.

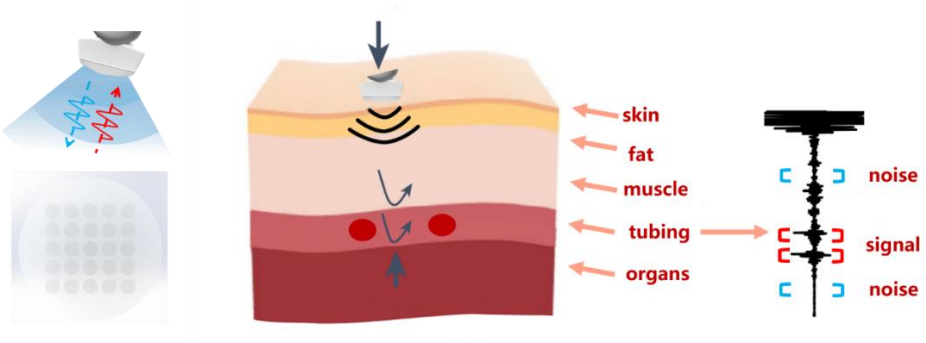

FIGURE 12. Schematic diagram of the CPC signal under the ultrasonic probe.

As shown in the Figure 13. The results show that in an ideal water medium, the CPC-A echo envelope is stronger and more stable compared to the one without periodic structural references, and the SNR maintains an advantage in multiple repetitions. This proves that the enhancement stems from the structural mechanism of "periodic hole array +Bragg band gap" rather than being solely determined by the material or geometric dimensions. After the sample was placed in the catheter, the flexible CPC (such as D) was close to the echo SNR in the exposed state within the catheter, suggesting that the catheter shell had a limited influence on its backreflection. When the medium (gas/liquid) inside and outside the conduit is changed, the overall variation of the visible echo and noise is mainly manifested as the baseline rise/attenuation caused by the difference in interface impedance, but the relative difference between CPC and the reference remains. After replacing the medium from water to the tissue-equivalent bulk mold, the overall SNR decreased, which was in line with the expectation of enhanced scattering and absorption. However, the relative advantages of CPC can still be distinguished, providing a preliminary basis for its availability under real organizational conditions.

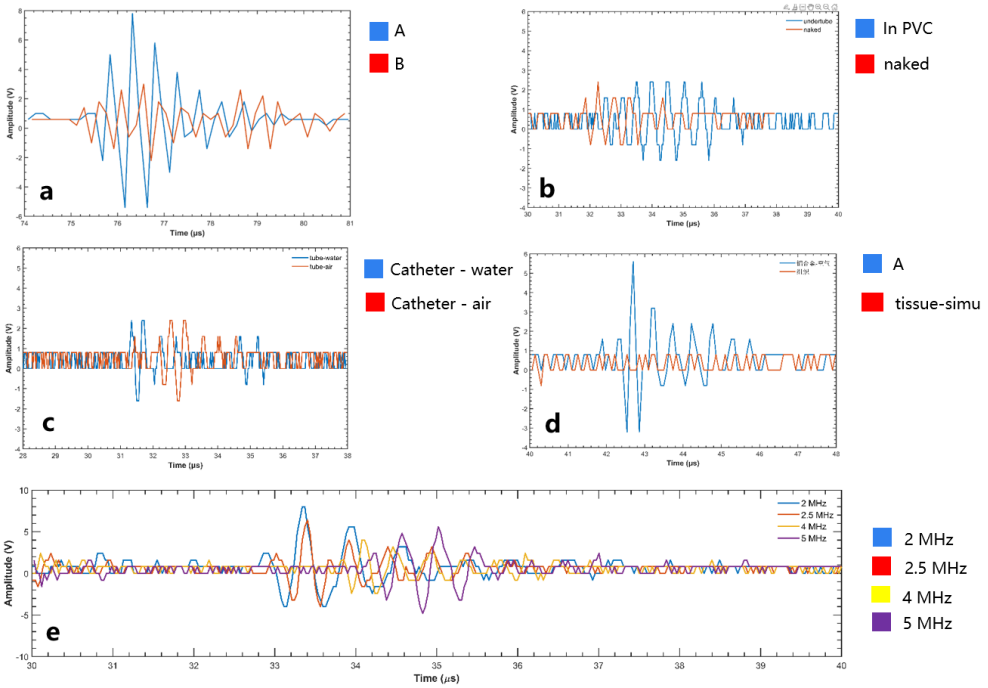

FIGURE 13. Signals of different structures under ultrasonic probes. a, signal comparison between underwater A and B; Signal comparison of b and D in the exposed state and within the catheter; c, signal comparison of the media inside the conduit being water and air respectively; Signal comparison of d, A and analog tissues; Signal comparison of e and A under 2.0MHz/2.5MHz/4.0MHz/5.0 MHz probes.

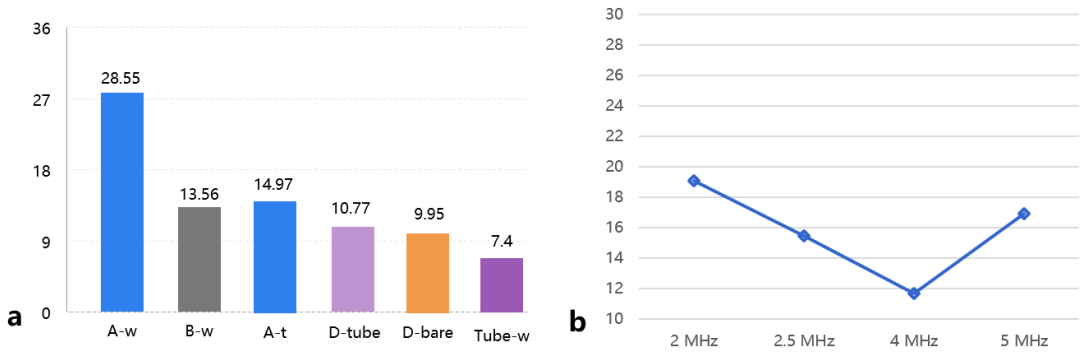

FIGURE 14. (a) SNR（dB）primary comparisons; (b) SNR of A across different frequencies.

Under frequency scanning, the SNR and frequency of CPC-A show A typical trend of "first decreasing and then increasing “: reaching a relatively high value at the low-frequency point (such as approximately 2 MHz), dropping to a low point in the mid-frequency band (such as approximately 4 MHz), and recovering somewhat at the high-frequency end (such as approximately 5 MHz). This trend corresponds to the transmission spectrum TL(ω) obtained from simulation and the band gap position: the transmission suppression and backscattering enhancement near the band gap are manifested in the time domain as more concentrated energy and improved echo SNR. The reference sample does not show the corresponding peak at the same frequency point. Spectral analysis further revealed that the echo energy of CPC showed significant peaking in the bandgap-related frequency band, while the spectral lines of the control sample were more dispersed or had no obvious peaks. These pieces of evidence collectively support the mechanism hypothesis of "frequency-selective reflection labeling".

To closely resemble the in vivo scenario, we built a silicone mold and cast Y-shaped channels to simulate blood vessels. We embedded aluminum/silicone/PDMS-air CPC in the triangular areas respectively as the test objects, and regarded the outside of the channels as "tissues". In this phantom, the echo delay of the CPC target is consistent with

the geometric depth and maintains a detectable SNR near its designed frequency band. The CPC of different materials varies in absolute magnitude, but they all have advantages over their respective non-periodic references. This indicates that within the frequency band that takes into account both penetration and resolution, CPC can provide stable characteristic signals for tip positioning through narrowband reflection.

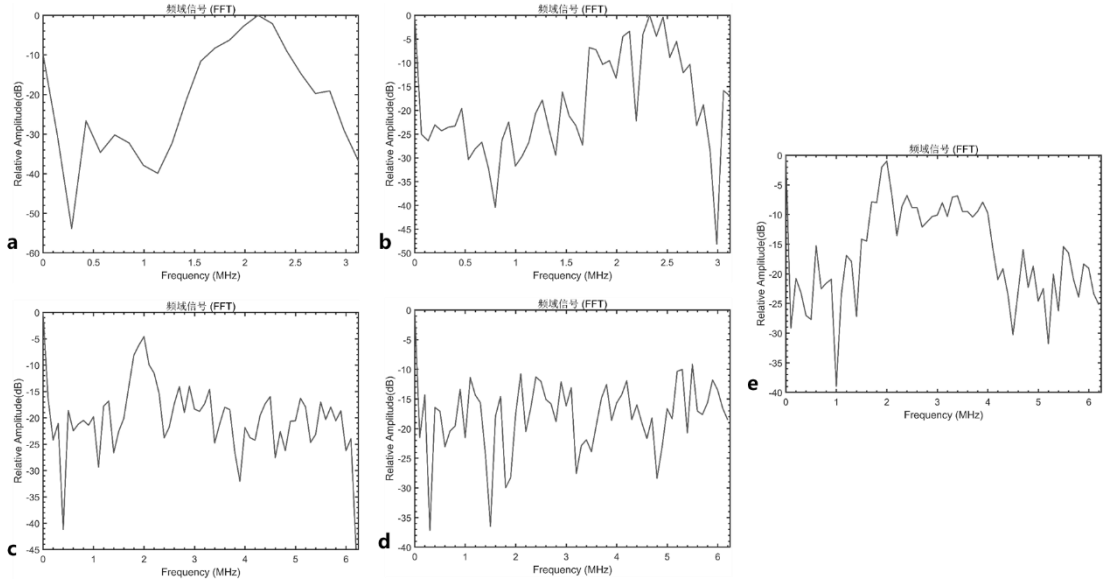

FIGURE 15. Frequency-domain signals after FFT. (a) the time-domain signal of structure A, in water; (b) the time-domain signal of structure B in water; (c) The time-domain signal of structure C, in the equivalent organization; (d) time-domain signal of equivalent organization; (e) the time-domain signal of structure A, in the equivalent organization.

In conclusion, the imaging link verified the intuitive visibility and intratuminal recognizability of CPC in the conventional B-mode; The echo link has demonstrated the structural reflection enhancement related to the band gap from both object specificity and frequency specificity aspects. Both of them are mutually verified with the simulated transmission loss spectrum TL(ω) in the frequency domain position, providing a systematic experimental basis for the application of "ultrasonic + passive phonon crystal labeling" in the tip positioning of ECMO intubation. Subsequently, we will integrate time, spectrum and phase information to establish a joint estimation model of "position + contact pressure", further enhancing the robustness under complex body positions and force conditions.

CONCLUSION

In this study, ultrasound was used as the imaging platform, and the Bragg bandgap of phonon crystals was utilized to achieve frequency-selective reflection labeling. Under the conventional B-mode, the image contrast at the catheter tip was significantly enhanced, and the spectral characteristics consistent with the bandgap were presented in the pulse-echo link. Finite element band and finite period transmission simulation provided predictions for band gap position and transmission suppression. The experiments verified "object specificity" and "frequency specificity" in water and tissue equivalent volume models: echo energy peaks and SNR increases appeared near the band gap, while no period reference and random pore structures did not have corresponding peaks. After catheter implantation, CPC remained identifiable, and although CNR decreased, it was overall higher than that without periodic reference. These results collectively indicate that passive structural labeling based on CPC can provide a bedside deployment, simple process tip positioning enhancement path for high-risk scenarios such as VA-ECMO without relying on contrast agents and ionizing radiation. This work also has certain limitations, mainly reflected in the following aspects: single-segment phonon crystals usually only provide 1-2 main band gaps within the target frequency band, making it difficult to cover all clinical presets of 1-5 MHz. This paper conducts feasibility verification using single-segment CPC. The engineering strategy of using multi-segment distributed CPC for frequency band completion still needs to be verified more systematically. The robustness of angles and orientations was only verified under limited conditions in this experiment. A complete multi-angle scan and statistical analysis are still needed to define the "Angle tolerance".

In addition to positioning, we observed that the flexible CPC is highly sensitive to contact pressure and surrounding hydrostatic pressure, which is manifested as measurable and resettable drift of the band gap center frequency. This "pressure-frequency" coupling characteristic provides a physical basis for force feedback: under known material and geometric conditions, pressure can be mapped to a bandgap (or echo spectrum peak) shift, thereby converting the contact force/adhesion state into quantifiable frequency readings. Next, we will conduct research on calibration curves and drift compensation, and collaborate with real-time UI/ human factors processes to explore the joint estimation of "position + force", targeting portable usage scenarios in ambulances, battlefields, and disaster sites.

ACKNOWLEDGMENTS

This work was completed in the laboratory of the Department of Mechanical Engineering at Tsinghua University. We sincerely thank the classmates and teachers in the research group for their strong support during the working period. Special thanks go to Teacher Zhang Xiangjun for his meticulous guidance in terms of research ideas, experimental design and presentation writing. All viewpoints and conclusions in the article are solely those of the author and have nothing to do with the individual being thanked.

REFERENCES

1. M.J. Jeon, A.C. Gordon, A.C. Larson, et al., Transcatheter intra-arterial infusion of doxorubicin loaded porous magnetic nano-clusters with iodinated oil for the treatment of liver cancer, Biomaterials, **88**, 25–33 (2016). https://doi.org/10.1016/j.biomaterials.2016.02.021
2. S. Miar, G. Gonzales, G. Dion, et al., Electrospun composite-coated endotracheal tubes with controlled siRNA and drug delivery to lubricate and minimize upper airway injury, Biomaterials, **309**, 122602 (2024). https://doi.org/10.1016/j.biomaterials.2024.122602
3. G. Douflé, L. Dragoi, D. Morales Castro, et al., Head-to-toe bedside ultrasound for adult patients on extracorporeal membrane oxygenation, Intensive Care Med, **50**, 632–645 (2024). https://doi.org/10.1007/s00134-024-07333-7
4. V.M. Bazan, E.M. Taylor, T.M. Gunn, et al., Overview of the bicaval dual lumen cannula. Indian J Thorac Cardiovasc Surg, **37**, 232–240 (2021). https://doi.org/10.1007/s12055-020-00932-1
5. L. Wang, N.E. Oyunbaatar, Y.J. Jeong, et al., The PolyCraft Polymer–Metal Hybrid Smart Stent System: The Future of Cardiovascular Blood Pressure Management, Adv. Funct. Mater., **34**, 2408022 (2024). https://doi.org/10.1002/adfm.202408022
6. G. Lafçı, A.B. Budak, A.Ü. Yener, O.F. Cicek, Use of extracorporeal membrane oxygenation in adults, Heart Lung Circ., **23**, 10–23 (2014). https://doi.org/10.1016/j.hlc.2013.08.009
7. M.G. Davies, J.P. Hart, Current status of ECMO for massive pulmonary embolism. Front. Cardiovasc. Med., **10**, 1298686 (2023). https://doi.org/10.3389/fcvm.2023.1298686
8. E. Lüsebrink, L. Binzenhöfer, D. Hering, et al., Scrutinizing the role of venoarterial extracorporeal membrane oxygenation: Has clinical practice outpaced the evidence? Circulation, **149**, 1033–1052 (2024). https://doi.org/10.1161/CIRCULATIONAHA.123.067087
9. M.D. Jarboe, et al., Avalon catheters in pediatric patients requiring ECMO: Placement and migration problems. J. Pediatr. Surg., **53**, 159–162 (2018). https://doi.org/10.1016/j.jpedsurg.2017.10.036
10. S.K. Pooboni, K.M. Gulla, Vascular access in ECMO, Indian J Thorac Cardiovasc Surg, **37**, 221–231 (2021). https://doi.org/10.1007/s12055-020-00999-w
11. A.K. Pillai, Z. Bhatti, A.J. Bosserman, et al., Management of vascular complications of extra-corporeal membrane oxygenation, Cardiovasc. Diagn. Ther., **8**, 372 (2018). https://doi.org/10.21037/cdt.2018.01.11
12. F. Yang, D. Hou, J. Wang, et al., Vascular complications in adult postcardiotomy cardiogenic shock patients receiving venoarterial extracorporeal membrane oxygenation, Ann. Intensive Care, **8**, 72 (2018). https://doi.org/10.1186/s13613-018-0417-3
13. C. Siems, R.J. Valentine, Q. Wang, J. Duke, M. Brunsvold, A.B. Reed, Risk factors for lower extremity vascular complications in adult patients on veno-arterial extracorporeal membrane oxygenation, J. Vasc. Surg., **77**, 1174–1181 (2023). https://doi.org/10.1016/j.jvs.2022.11.047

14. I. Gulkarov, E. Khusid, B. Worku, et al., Meta-analysis of the effect of vascular complications on mortality in patients undergoing femoral venoarterial extracorporeal membrane oxygenation, Ann. Vasc. Surg., **71**, 488–495 (2021). https://doi.org/10.1016/j.avsg.2020.09.042
15. S. Nazarian, A. Kolandaivelu, M.M. Zviman, et al., Feasibility of real-time magnetic resonance imaging for catheter guidance in electrophysiology studies, Circulation, **118**, 223–229 (2008). https://doi.org/10.1161/CIRCULATIONAHA.107.742452
16. Z. Dong, et al., Shape tracking and feedback control of cardiac catheter using MRI-guided robotic platform—validation with pulmonary vein isolation simulator in MRI, IEEE Trans. Robot., **38**, 2781–2798 (2022). https://doi.org/10.1109/TRO.2022.3154691
17. R.J. Lederman, M.A. Guttman, D.C. Peters, et al., Catheter-based endomyocardial injection with real-time magnetic resonance imaging, Circulation, **105**, 1282–1284 (2002). https://doi.org/10.1161/01.cir.0000012425.71261.fc
18. J.R. Tse, E.R. Felker, G. Tse, et al., Colonoscopy versus catheter angiography for lower gastrointestinal bleeding after localization on CT angiography, J. Am. Coll. Radiol., **19**, 513–520 (2022). https://doi.org/10.1016/j.jacr.2022.01.010
19. Y. Fang, F. Yang, W. He, et al., Intravascular catheter navigation and thrombus localization using hybrid electrodes electric field stereotaxis, Measurement, **250**, 117169 (2025). https://doi.org/10.1016/j.measurement.2025.117169
20. X.L. Deán-Ben, J. Robin, D. Nozdriukhin, et al., Deep optoacoustic localization microangiography of ischemic stroke in mice, Nat. Commun., **14**, 3584 (2023). https://doi.org/10.1038/s41467-023-39069-1
21. S. Liu, Y. Wang, X. Yang, et al., Deep learning in medical ultrasound analysis: A review, Engineering, **5**, 261–275 (2019). https://doi.org/10.1016/j.eng.2018.11.020
22. J.A. Noble, D. Boukerroui, Ultrasound image segmentation: a survey, IEEE Trans. Med. Imaging, **25**, 987–1010 (2006). https://doi.org/10.1109/TMI.2006.877092
23. L.J. Salomon, N. Winer, J.P. Bernard, Y. Ville, A score-based method for quality control of fetal images at routine second-trimester ultrasound examination, Prenat. Diagn., **28**, 822–827 (2008). https://doi.org/10.1002/pd.2016
24. S. Zhao, X. Zhang, K. Bailey, et al., Label-free dual-modal photoacoustic/ultrasound localization imaging for studying acute kidney injury, Adv. Sci., **12**, 2414306 (2025). https://doi.org/10.1002/advs.202414306
25. I. Spanuchart, T. Supachokchaiwattana, K. Thammavaranucupt, et al., Tangential biopsy angle and needle depth for adequacy and safety outcomes in ultrasound-guided native kidney biopsy—a single-center experience in a high-risk population, J. Nephrol., **38**, 1947-1955 (2025). https://doi.org/10.1007/s40620-025-02362-x
26. X. Gao, X. Chen, M. Lin, et al., A wearable echomyography system based on a single transducer, Nat. Electron., **7**, 1035–1046 (2024). https://doi.org/10.1038/s41928-024-01271-4
27. H. Hu, H. Huang, M. Li, et al., A wearable cardiac ultrasound imager, Nature, **613**, 667–675 (2023). https://doi.org/10.1038/s41586-022-05498-z
28. R. Chiletti, W. Butt, G. MacLaren, Rapid deployment ECMO, Curr. Treat. Options Peds, **1**, 4–14 (2015). https://doi.org/10.1007/s40746-014-0010-4
29. J.J. Hawley, S.L. Allen, et al., Commercially available ultrasound contrast agents: factors contributing to favorable outcomes with ultrasound-mediated drug delivery and ultrasound localization microscopy imaging. Invest. Radiol., **60**, 813-822 (2025). https://doi.org/10.1097/RLI.0000000000001197
30. D.J. Widder, J.F. Simeone, Microbubbles as a contrast agent for neurosonography and ultrasound-guided catheter manipulation: in vitro studies, Am. J. Roentgenol., **147**, 347–352 (1986). https://doi.org/10.2214/ajr.147.2.347
31. R. da Hora Passos, et al., Agitated saline bubble–enhanced ultrasound for assessing appropriate position of hemodialysis central venous catheter in critically ill patients, Kidney Int. Rep., **2**, 952–956 (2017). https://doi.org/10.1016/j.ekir.2017.03.010
32. M.A. Wheatley, B. Schrope, P. Shen, Contrast agents for diagnostic ultrasound: development and evaluation of polymer-coated microbubbles, Biomaterials, **11**, 713–717 (1990). https://doi.org/10.1016/0142-9612(90)90033-M
33. O. Trushkevych, V. Reshetnyak, M. Turvey, R. S. Edwards, Polymer-dispersed liquid-crystal coatings for ultrasound visualization: Experiment and theory, Phys. Rev. E, **109**, 064701 (2024). https://doi.org/10.1103/PhysRevE.109.064701
34. 34. Michel Versluis et al. Ultrasound Contrast Agent Modeling: A Review, Ultrasound in Medicine and Biology, **46**, 2117–2144 (2020). https://doi.org/10.1016/j.ultrasmedbio.2020.04.014

35. Kagan D, Benchimol MJ, et al. Acoustic droplet vaporization and propulsion of perfluorocarbon-loaded microbullets for targeted tissue penetration and deformation, Angew Chem Int Ed, **51**, 7519–7522 (2012). https://doi.org/10.1002/anie.201201902
36. van de Berg, Nick J., et al. A Methodical Quantification of Needle Visibility and Echogenicity in Ultrasound Images, Ultrasound in Medicine and Biology, **45**, 998–1009 (2019). https://doi.org/10.1016/j.ultrasmedbio.2018.10.004
37. C.H. Hovgesen, J.E. Wilhjelm, P. Vilmann, E. Kalaitzakis. Echogenic surface enhancements for improving needle visualization in ultrasound, Journal of Ultrasound in Medicine, **41**, 311–325 (2022). https://doi.org/10.1002/jum.15713
38. K. Bishop, Living bandgaps, Nature Materials, **16**, 786–787 (2017). https://doi.org/10.1038/nmat4947
39. 王瑁成, 有限单元法, 北京: 清华大学出版社, 2003. https://wqbook.wqxuetang.com/book/7106
40. M. I. Hussein, C.N. Tsai, H. Honarvar, Thermal conductivity reduction in a nanophononic metamaterial versus a nanophononic crystal: A review and comparative analysis, Advanced Functional Materials, **30**, 1906718 (2020). https://doi.org/10.1002/adfm.201906718.